Asymmetric Rolling of TZ73 Magnesium Alloy to Improve Its Ductility

Krishna Kamlesh Verma, Satyam Suwas, and Subodh Kumar

Abstract

Asymmetric rolling, i.e., upper and lower rolls having different circumferential speeds, is a novel technique to improve the ductility of Mg alloys. A newly developed TZ73 Mg alloy was squeeze cast, homogenized at 300 °C for 24 h, rolled at 350 °C by symmetric and asymmetric rolling, and annealed at 215 °C for 30 min. The microstructure was characterized by X-ray diffraction, scanning electron microscope equipped with energy-dispersive X-ray spectroscopy and electron backscattered diffraction. A weakening of basal texture with a concomitant increase in ductility was observed for asymmetrically rolled sheet while retaining the same strength as in symmetrically rolled sheet. Thus, tensile properties of 0.2% PS = 290 MPa, UTS = 332 MPa and El = 13% in hot rolled, and 0.2% PS = 182 MPa, UTS = 282 MPa and El = 21% in annealed condition were obtained for asymmetrically rolled sheet, which are extremely good for a rolled Mg alloy sheet.

Keywords

Mg alloys • Asymmetric rolling • Microstructure • Crystallographic texture • Tensile properties

Introduction

Mg-based alloys find wide applications in the automobile, aerospace, and electronics industries due to its low density, high specific strength, excellent machinability, and castability. The lightest structural Mg-based alloys reduce the greenhouse effect and enhance fuel efficiency [1–3]. However, Mg-based alloys in wrought processing conditions find limited applications due to its poor strength and limited formability at room temperature because of its hexagonal closed packed (HCP) crystal structure [4]. According to von Mises criterion, minimum five independent slip systems are required for the uniform plastic deformation of a polycrystalline material. For Mg, at room temperature deformation, basal $(0001)<11\bar{2}0>$ slip system dominates, which has minimum critical resolved shear stress (CRSS) value. The basal slip system has only two independent slip systems, which causes limited formability [5, 6].

For the development of high-strength and cost-effective Mg-based alloys, Mg–Sn alloy system has received attention as a promising candidate in the cast and wrought processing conditions. In Mg–Sn binary alloy system, the Mg_2Sn intermetallic phase has a high melting temperature (770 °C), which is comparable to precipitates formed in Mg-RE-based alloys. The growth of dynamically recrystallized grains can be suppressed by effective grain boundary pinning by the fine Mg_2Sn particles [7–9]. The presence of dynamically precipitated Mg_2Sn particles at the grain boundary as well as within the grains leads to excellent tensile properties at room temperature. The strength of Mg–Sn-based alloys is enhanced with increasing Sn content but deteriorates its ductility due to the formation of a semi-continuous type of network at the grain boundary by the Mg_2Sn phase. Liu et al. [8] reported that the optimum addition of the Sn in Mg–Sn-based alloys system is 5–7 wt.%. It is reported that Zn in solid solution improves strength and ductility for the Mg–Sn-based alloys [7, 9]. Therefore, for the present study, Zn was added as the third alloying element.

A strong basal texture is developed during the rolling process, which diminishes its ductility and formability [10, 11]. The weakening of basal texture leads to improvement in ductility and formability at room temperature. It has been reported that the introduction of shear stresses during deformation could lead to the modification of the

K. K. Verma · S. Suwas · S. Kumar (✉)
Department of Materials Engineering,
Indian Institute of Science, Bangalore, 560012, India
e-mail: skumar@iisc.ac.in

K. K. Verma
e-mail: krishnakamlesh.iisc14@gmail.com

S. Suwas
e-mail: satyamsuwas@iisc.ac.in

© The Minerals, Metals & Materials Society 2020
J. B. Jordon et al. (eds.), *Magnesium Technology 2020*, The Minerals, Metals & Materials Series, https://doi.org/10.1007/978-3-030-36647-6_30

crystallographic texture in the rolled sheet [12, 13]. The asymmetric rolling (ASR) process is an effective method to improve ductility and formability of Mg-based alloys by introducing shear stresses and weakening the basal texture [14]. In the ASR process, the circumferential speeds of the upper and lower rollers are different, so the shear deformation is applied throughout the thickness of the sheet [15, 16]. In the present study, the homogenized TZ73 alloy is subjected to ASR and conventional symmetric rolling (SR) at 350 °C. For the ASR process, the circumferential speeds of the upper and lower rollers are selected as 0.03 m s^{-1} and 0.15 m.s^{-1} (speed ratio 1 : 5), respectively. For the SR process, the circumferential speed of both the rollers is 0.09 m s^{-1} (speed ratio 1 : 1). The hot rolled sheets are annealed at 215 °C for 30 min. The rolled sheets are investigated in two conditions: (i) hot rolled (HR) and (ii) hot rolled and annealed (HRA). The microstructure, texture, and tensile behaviour are studied for ASR and SR processed sheets.

Experimental Details

Commercially pure Mg (>99.80 wt.%), Sn (>99.97 wt.%), and Zn (>99.98 wt.%) ingots were charged into a graphite crucible and melted at 720 °C in a resistance pit furnace. The complete melting and casting were carried out under a protective argon gas atmosphere. Squeeze casting was adopted as the casting technique to refine the as-cast microstructure, in which the hot metal was poured into the preheated (200 °C) cylindrical die (∅75 × 75 mm^2) and a pressure of 100 MPa was applied till the completion of solidification. The obtained alloy composition was determined to be Mg–6.9Sn–2.6Zn and designated as TZ73 according to ASTM standard nomenclature. The plates of dimensions 10 × 30 × 50 mm^3 were machined from the cylindrical cast ingot for hot rolling. Prior to hot rolling, the as-cast plates were homogenized at 300 °C for 24 h (hereafter the homogenized samples will be designated as H300) and hot rolled at 350 °C to 1-mm-thick sheets. The thickness reduction of 80% was achieved in multiple passes. The hot rolled sheets were annealed at 215 °C for 30 min. The rolled sheets were investigated in two conditions: (i) hot rolled (HR) and (ii) hot rolled and annealed (HRA). The flat tensile specimens of the dimension 10 × 2 × 1 mm^3 were machined via electron discharge machine (EDM) with the gauge length parallel to the rolling direction (RD), and tested on an INSTRON-5967 machine at room temperature and 1×10^{-3} s^{-1} strain rate. The standard metallographic techniques were adopted for microstructural analysis. The polished specimens were etched for 5 s using acetic-picral (1.5 g picric acid, 1.2 ml acetic acid, 2.5 ml distilled water, and 25 ml ethanol). The microstructure was examined under a scanning electron microscope (FEI-ESEM Quanta 200) and electron probe micro-analyser (EPMA-JEOL-JXA-8530F) equipped with energy-dispersive X-ray spectroscopy (EDS) and wavelength dispersive X-ray spectroscopy (WDS). X'Pert Pro PANalytical diffractometer using CuK_α radiation (λ = 0.154 nm) was used to identify the different phases present in the alloy. For the detailed microstructural and microtexture investigation, electron backscatter diffraction (EBSD) scan was recorded using advanced focused ion beam system (HELIOS G4 UX).

Results and Discussion

Phase Analysis and Microstructural Characterization

The XRD patterns for H300, SR, and ASR samples in HR condition are shown in Fig. 1. It reveals the presence of Mg and Mg_2Sn phases in the TZ73 alloy. The highest peak intensity of Mg for the H300 sample was observed for pyramidal $(10\bar{1}1)$ planes, whereas, for SR and ASR samples, the highest peak intensity for Mg was observed for basal (0002) planes. Thus, the alloy gets textured after rolling; i.e., the basal plane normals are preferentially oriented perpendicular to rolling direction (RD).

Figure 2 represents the SEM micrographs for H300, SR, and ASR samples. Figure 2a shows that the H300 microstructure primarily consists of cells, with dendritic features at a few places, and Mg_2Sn particles along the cell boundaries. Figure 2b shows that Mg_2Sn particles get fragmented and aligned along RD for the SR sample. However, for the ASR sample, the shear stresses were introduced during deformation, which changes the material flow direction and alignment direction of Mg_2Sn particles (Fig. 2c).

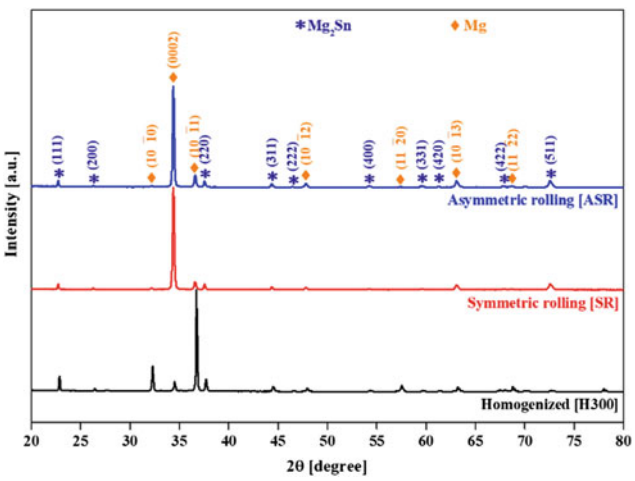

Fig. 1 X-ray diffraction pattern of TZ73 alloy

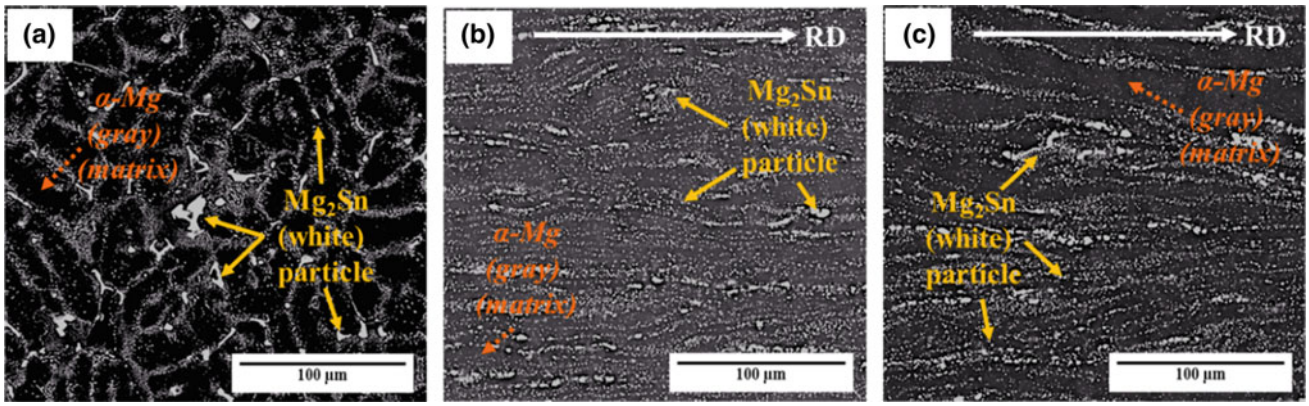

Fig. 2 Backscattered scanning electron (SEM-BSE) micrographs **a** H300, **b** SR, and **c** ASR samples in HR condition

The distributed fine Mg_2Sn particles act as a nucleating site as well as a barrier to suppress the growth of the dynamically recrystallized (DRX) grains [17, 18]. The intense plastic strain was imposed on the entire sample during ASR deformation. An equation for the strain (ε) imposed by ASR is proposed as follows [19]:

$$\varepsilon = \frac{2}{\sqrt{3}}\sqrt{\left[1+\left\{\frac{(1-r)^2}{r(2-r)}\tan(\theta)\right\}^2\right]}\ln\left(\frac{1}{1-r}\right) \quad (1)$$

$$r = 1-\left(\frac{T_f}{T_i}\right) \quad (2)$$

where T_i and T_f are the initial and final thicknesses of the sample before and after rolling and angle θ is the apparent shear angle ($\theta = 69°$) caused by ASR. For the conventional SR, a true strain of 1.61 has been evaluated on the rolled sheet. However, for the ASR, in addition to the true strain, a shear strain of 1.86 is also imposed on the ASR sheet. The concomitant high shear stress significantly affects the texture and consequently tensile properties.

Microstructural Characterization by EBSD

Figures 3 and 4 illustrate the EBSD maps for the SR and ASR processes in HR condition. The EBSD scan was carried out on the cross section (TD plane) of the rolled sheet. Figures 3a and 4a show the inverse pole figure (IPF) maps for SR and ASR processes. The IPF maps represent the orientation of the grains with respect to the sample frame of reference. Figures 3b and 4b represent grain boundary (GB) maps superimposed on the image quality (IQ) maps for SR and ASR processes. The low-angle grain boundaries (LAGBs) and high-angle grain boundaries (HAGBs) were calculated from the GB + IQ maps. Figures 3c and 4c show the grain orientation spread (GOS) maps for SR and ASR processes. The GOS maps represent the distribution of recrystallized and deformed grains. The fraction of dynamically recrystallized (DRX) and deformed grains were evaluated from the GOS maps. In order to ascertain the partitioning between recrystallized and deformed grains, three considerations were taken into account: (i) The DRX grains should be equiaxed with aspect ratio close to 1, while the deformed grains should be elongated with a high aspect ratio, (ii) the deformed grains should possess a high fraction of LAGBs and the recrystallized grains should have a low fraction of LAGBs, and (iii) in the texture criteria, the DRX grain in the hexagonal crystal is rotated by $\sim 30°$ around <0001> with respect to the deformed grain [20, 21]. Therefore, the texture obtained from the partitioned DRX grains should show maximum $\sim 30°$ rotation and spread in pole figure (PF) and orientation distribution function (ODF), respectively. For the recrystallized grain and deformed grain fraction, the misorientation of $\leq 2.5°$ and $>2.5°$ has been considered for recrystallized and deformed grains, respectively, and Figs. 3d and 4d represent the kernel average misorientation (KAM) plots for SR and ASR processes. The KAM value represents the local variation in misorientation. The average misorientation between a point in the scan and the average misorientation value is assigned as the KAM value. The number fraction is plotted as a function of the KAM values, and the overall KAM value is reported in Table 1. Figures 5 and 6 represent the IPF, GB + IQ, GOS, and KAM maps for the SR and ASR processes in HRA condition.

Table 1 shows all the values derived from EBSD scans for SR and ASR processes in HR and HRA conditions. It is observed that in the HR condition, the ASR process yields slightly finer grains, a higher fraction of LAGBs, almost the same fraction of DRX grains, and a higher KAM value, as compared to the SR process. After annealing treatment, the average grain size is reduced, fraction of HAGBs is

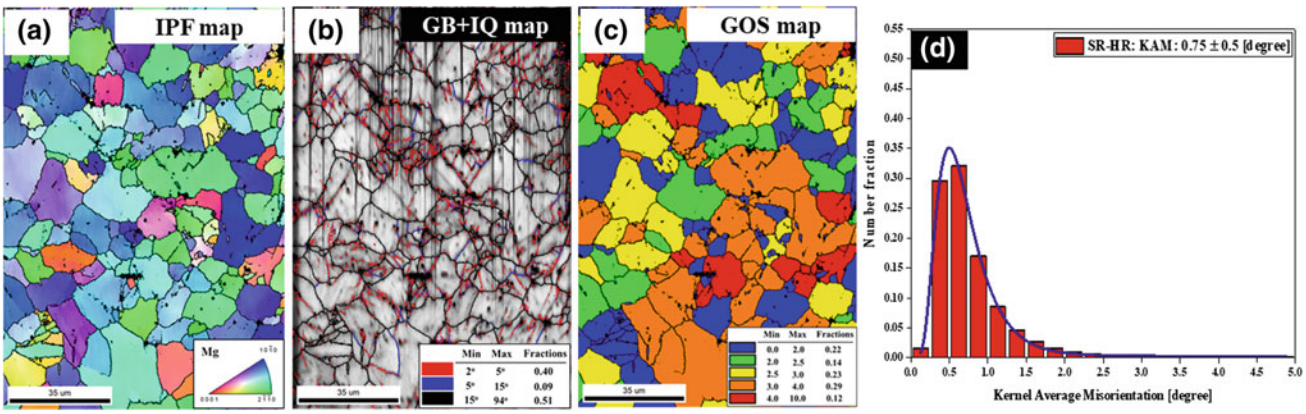

Fig. 3 EBSD maps for SR in HR condition **a** IPF map, **b** IQ map, **c** GOS map, and **d** KAM plot

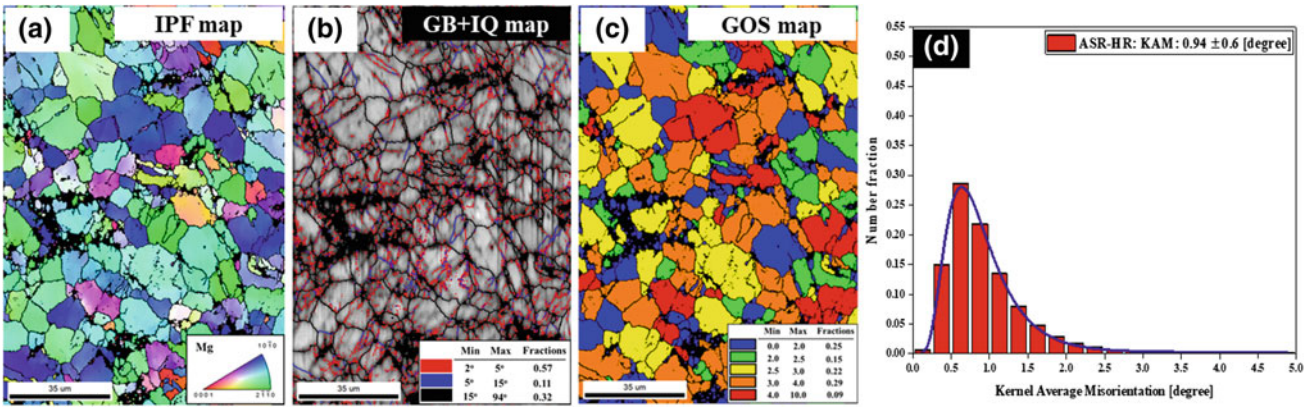

Fig. 4 EBSD maps for ASR in HR condition **a** IPF map, **b** IQ map, **c** GOS map, and **d** KAM plot

Table 1 Comparison between SR and ASR processes in HR and HRA conditions

Processing conditions				
	SR-HR	ASR-HR	SR-HRA	ASR-HRA
Grain size (μm)	13.9	11.2	11.9	10.5
LAGBs (%)	49	68	26	20
HAGBs (%)	51	32	74	80
Recrystallized grain (%)	36	40	88	91
KAM	0.76°	0.94°	0.58°	0.57°

increased, fraction of recrystallized grains is increased, and KAM value is decreased, for both the SR and ASR processes. Thus, the difference in all the values between SR and ASR processes is reduced in HRA condition.

For the ASR process, in addition to the true strain, a shear strain of 1.86 is also imposed. Due to higher shear strain introduced during ASR, the higher strain gradient, hence higher KAM value is obtained as compared to SR process in HR condition. In addition to that, the fine Mg_2Sn particles near grain boundaries, which act as a nucleating site and a barrier to suppress the growth of DRX grains, promote the formation of fine recrystallized grains [22]. This leads to finer grain size in ASR as compared to SR process in HR condition. It has been reported that the deformed grains should possess a high fraction of LAGBs and the recrystallized grains should have a low fraction of LAGBs [21]. Therefore, ASR exhibits higher fraction of LAGBs as compared to SR process in HR condition. After annealing at 215 °C, the strain gradient is reduced, which results in recrystallization of the deformed microstructure. The new fine recrystallized grains formed after annealing treatment lead to further refinement in grain size for both the SR and ASR processes. The KAM values for both the SR and ASR processes are reduced on annealing as strained regions are

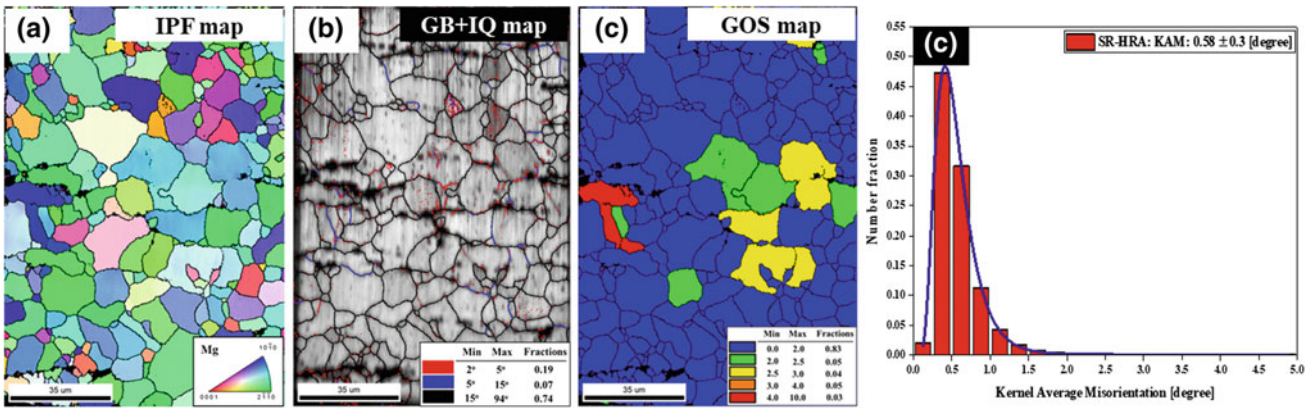

Fig. 5 EBSD maps for SR in HRA condition **a** IPF map, **b** IQ map, **c** GOS map, and **d** KAM plot

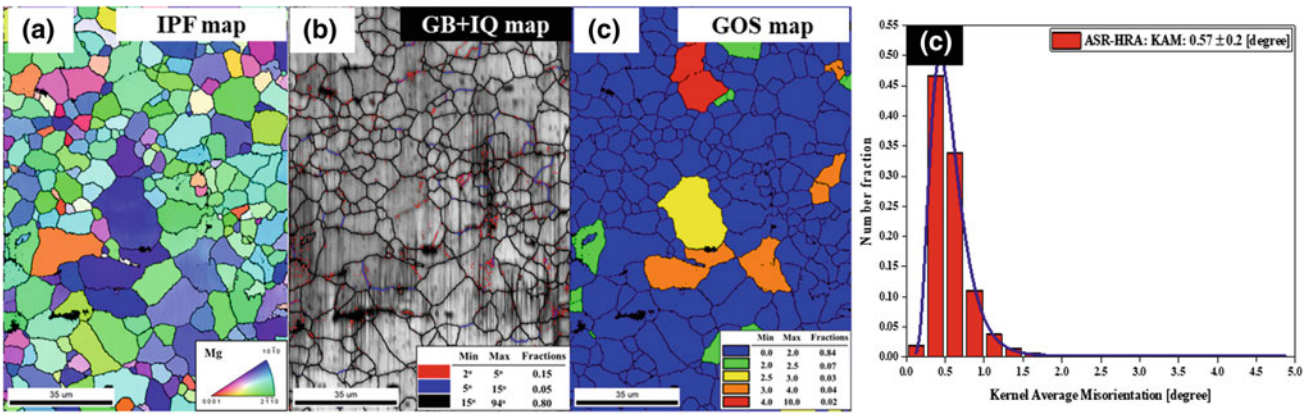

Fig. 6 EBSD maps for ASR in HRA condition **a** IPF map, **b** IQ map, **c** GOS map, and **d** KAM plot

converted into recrystallized grains and LAGBs are converted into HAGBs.

Crystallographic Texture Evolution

Figure 7a, e and b, f illustrate the basal (0002) and prismatic $(10\bar{1}0)$ pole figures (PFs) for SR and ASR processes, respectively, in HR condition. It is observed that both the processes result in basal texture after hot rolling. For the SR sample, the maximum basal pole intensity is calculated to be 18.8 (Fig. 7a). Along with $\{0001\}<11\bar{2}0>$ an additional $\{0001\}<10\bar{1}0>$ texture component is observed in $(10\bar{1}0)$ PF (Fig. 7b). However, for the ASR sample, the maximum basal texture intensity is reduced to 12.6 (Fig. 7e). The intensity of $\{0001\}<11\bar{2}0>$ and $\{0001\}<10\bar{1}0>$ texture components is also reduced in ASR (Fig. 7f) as compared to SR process. The basal pole intensity spread $\sim 30°$ is similar for both the SR and ASR processes, which exhibit a similar fraction of DRX grains in HR condition. Figure 7c, d and g, h show the $\varphi_2 = 0°$ and 30° sections of the ODFs for SR and ASR processes, respectively, in HR condition. The presence of a continuous basal fiber is clearly visible in the ODF sections with maxima at the location of texture components $\{0001\}<11\bar{2}0>$ and $\{0001\}<10\bar{1}0>$ for the SR and ASR processes. However, the intensity is reduced for ASR as compared to the SR process. The spreading of basal fiber towards ϕ angle $\sim 30°$ is similar for both the SR and ASR processes.

Figure 8a, e and b, f show the (0002) and $(10\bar{1}0)$ PFs for SR and ASR processes, respectively, in HRA condition. It is observed that the basal texture intensity is further reduced on annealing treatment. The maximum basal texture intensity is reduced to 16.5 for SR (Fig. 8a) and 9.2 for ASR process (Fig. 8e). Thus, the maximum basal texture intensity remains lower for ASR process in HRA condition as well. Additionally, $\{0001\}<11\bar{2}0>$ and $\{0001\}<10\bar{1}0>$ texture components are observed in $(10\bar{1}0)$ PFs with a lower intensity for ASR as compared to SR process in HRA condition (Fig. 8b, f). Figure 8c, d and g, h represent the $\varphi_2 = 0°$ and 30° ODFs sections for SR and ASR processes, respectively, in HRA condition. It is observed that the ASR

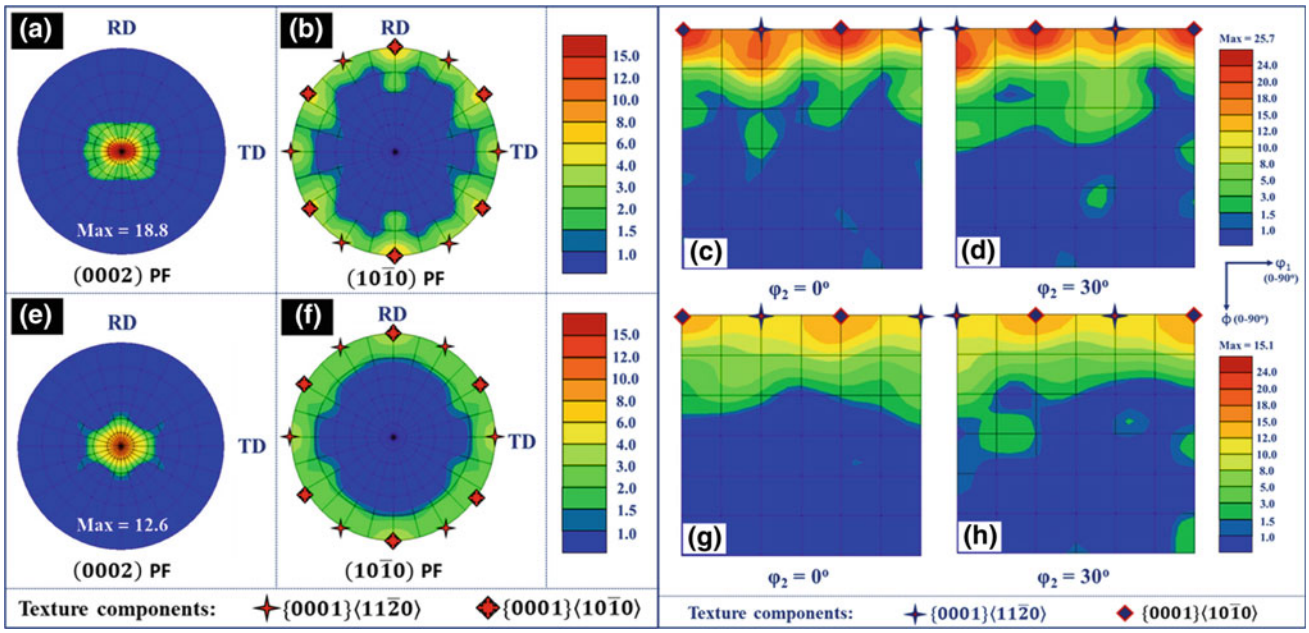

Fig. 7 PFs and ODFs for **a–d** SR and **e–h** ASR processes in HR condition

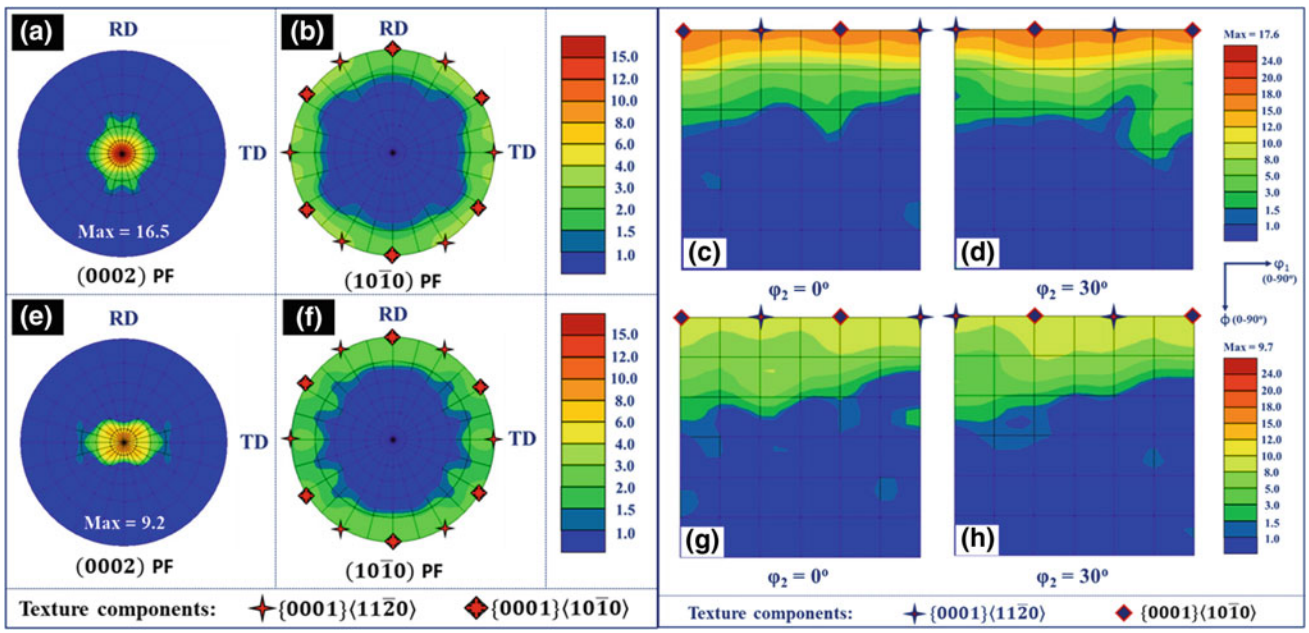

Fig. 8 PFs and ODFs for **a–d** SR and **e–h** ASR processes in HRA condition

process exhibits the presence of continuous basal fiber in the ODF sections with the weakened texture intensity. The intensity for the texture components $\{0001\}<11\bar{2}0>$ and $\{0001\}<10\bar{1}0>$ is observed to be lower for ASR as compared to the SR process. The spreading of basal fiber towards ϕ angle $\sim 30°$ is more for ASR as compared to SR process. Thus, ASR results in a weaker basal texture than SR process in HR condition. The basal texture gets further weakened on annealing, the basal texture still remaining weaker in ASR than SR process in HRA condition.

Crystallographic texture plays a significant role during the processing of Mg-based alloys. For Mg, the important slip systems are basal $\{0001\}<11\bar{2}0>$; prismatic $\{1\bar{1}00\}<11\bar{2}0>$; pyramidal-I $\{10\bar{1}1\}<11\bar{2}0>$ and $\{10\bar{1}2\}<11\bar{2}0>$; pyramidal-II $\{11\bar{2}2\}<11\bar{2}3>$ [20]. Each slip system gets activated when its critical resolved

shear stress (CRSS) is reached. Basal slip system is dominant at room temperature deformation because it has the lowest CRSS as compared to prismatic and pyramidal slip system. When the deformation temperature is higher than 250 °C, other non-basal slip systems also contribute significantly, which leads to higher formability for Mg alloys [23]. Several descriptions of deformation by ASR have been proposed [4, 24]. The shear stress is generated by the different circumferential velocities of the rollers during deformation [25]. The higher shear stress induced during ASR suppresses the basal texture. The weaker basal texture results in the activation of the non-basal slip, which leads to greater ductility and formability of Mg-based alloys [20, 23].

Tensile Properties

Figure 9a shows the true stress–true strain curves and the corresponding tensile properties are reported in Fig. 9b for TZ73 alloy along RD for SR and ASR processes in HR and HRA conditions. In HR condition, the ASR sample exhibits almost the same strength but 3% higher elongation to failure (El) than the SR sample. It is observed that strength is reduced and elongation to failure is increased after annealing treatment. The ASR sample again exhibits almost the same strength but 2% higher elongation to failure in HRA condition.

The tensile properties of the TZ73 alloy are mainly attributed to fine grain size and solid solution strengthening by dissolved Zn and Sn atoms in α-Mg matrix. During hot rolling highly thermally stable Mg_2Sn particles distributed along grain boundaries act as nucleation sites for DRX grains and preclude the DRX grain growth [17, 18]. The annealing treatment leads to further refinement of grains. The weaker basal texture obtained in the ASR results in higher ductility than SR process in both HR and HRA conditions.

Conclusions

The homogenized TZ73 alloy was hot rolled at 350 °C by SR and ASR processes followed by annealing at 215 °C for 30 min. The detailed investigations have been carried out to explore the microstructural, texture evolutions, and tensile properties. The analysis of the results led to the following main conclusions:

1. ASR is more effective process to introduce additional shear strain (1.86) along with true strain (1.61).
2. The ASR process yielded slightly finer grains, a higher fraction of LAGBs, almost the same fraction of DRX grains, and a higher KAM value as compared to the SR process in the HR condition.
3. After annealing treatment, the average grain size reduced, the fraction of HAGBs increased, fraction of recrystallized grains increased, and KAM value decreased, for both the SR and ASR processes.
4. The basal texture was weaker for ASR as compared to SR process in HR condition. The spreading of basal fiber towards ϕ angle $\sim 30°$ was similar for both the SR and ASR processes in HR condition.
5. The basal texture was further weakened on annealing, the ASR still exhibiting weaker basal texture than the SR process in HRA condition. The spreading of basal fiber towards ϕ angle $\sim 30°$ was more for ASR as compared to SR process in HRA condition.
6. In HR condition, the ASR sample exhibited almost the same strength but 3% higher elongation to failure

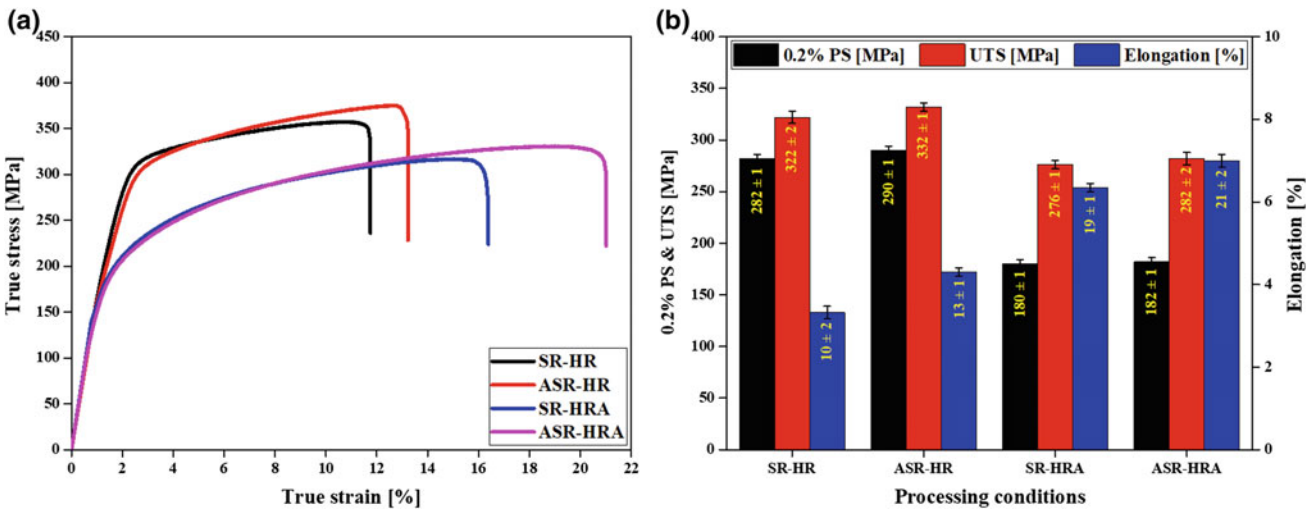

Fig. 9 **a** True stress–true strain curves and **b** tensile properties for TZ73 alloy

(El) than the SR sample. The strength was reduced and elongation to failure was increased after annealing treatment. The ASR sample again exhibited almost the same strength but 2% higher elongation to failure in HRA condition. The higher elongation in ASR process is attributed to the weaker basal texture.

7. Thus, tensile properties of 0.2% PS = 290 MPa, UTS = 332 MPa and El = 13% in HR and 0.2% PS = 182 MPa, UTS = 282 MPa and El = 21% in HRA condition were obtained for the newly developed TZ73 alloy by using ASR process, which are extremely good for a rolled Mg alloy sheet.

Acknowledgements The authors gratefully acknowledge the financial support from the Science and Engineering Research Board (SERB) of the Department of Science and Technology (DST), Government of India. The authors are grateful to Prof. S. Seshan for his help and guidance in squeeze casting.

References

1. B.L. Mordike, T. Ebert, Magnesium Properties - applications - potential, Mater. Sci. Eng. A (2001). https://doi.org/10.1016/s0921-5093(00)01351-4.
2. E. Aghion, B. Bronfin, D. Eliezer, The role of the magnesium industry in protecting the environment, J. Mater. Process. Technol. 117 (2001) 381–385. https://doi.org/10.1016/s0924-0136(01)00779-8.
3. E. Aghion, B. Bronfin, Magnesium Alloys Development towards the 21st Century, Mater. Sci. Forum. 350–351 (2000) 19–30. https://doi.org/10.4028/www.scientific.net/msf.350-351.19.
4. B. Beausir, S. Biswas, D.I. Kim, L.S. Tóth, S. Suwas, Analysis of microstructure and texture evolution in pure magnesium during symmetric and asymmetric rolling, Acta Mater. 57 (2009) 5061–5077. https://doi.org/10.1016/j.actamat.2009.07.008.
5. R.K. Sabat, S.K. Sahoo, D. Panda, U.K. Mohanty, S. Suwas, Orientation dependent recrystallization mechanism during static annealing of pure magnesium, Mater. Charact. 132 (2017) 388–396. https://doi.org/10.1016/j.matchar.2017.09.003.
6. S.V.S. Narayana Murty, N. Nayan, R. Madhavan, S.C. Sharma, K. M. George, S. Suwas, Analysis of Microstructure and Texture Evolution in Mg-3Al-1Zn Alloy Processed Through Groove Rolling, J. Mater. Eng. Perform. 24 (2015) 2091–2098. https://doi.org/10.1007/s11665-015-1459-4.
7. T.T. Sasaki, K. Yamamoto, T. Honma, S. Kamado, K. Hono, A high-strength Mg–Sn–Zn–Al alloy extruded at low temperature, Scr. Mater. 59 (2008) 1111–1114. https://doi.org/10.1016/j.scriptamat.2008.07.042.
8. H. Liu, Y. Chen, Y. Tang, S. Wei, G. Niu, The microstructure, tensile properties, and creep behavior of as-cast Mg-(1–10)%Sn alloys, J. Alloys Compd. 440 (2007) 122–126. https://doi.org/10.1016/j.jallcom.2006.09.024.
9. Y.K. Kim, S.W. Sohn, D.H. Kim, W.T. Kim, D.H. Kim, Role of icosahedral phase in enhancing the strength of Mg–Sn–Zn–Al alloy, J. Alloys Compd. 549 (2013) 46–50. https://doi.org/10.1016/j.jallcom.2012.09.050.
10. S. Biswas, D.-I. Kim, S. Suwas, Asymmetric and symmetric rolling of magnesium: Evolution of microstructure, texture and mechanical properties, Mater. Sci. Eng. A 550 (2012) 19–30. https://doi.org/10.1016/j.msea.2012.03.099.
11. H. Watanabe, T. Mukai, K. Ishikawa, Effect of temperature of differential speed rolling on room temperature mechanical properties and texture in an AZ31 magnesium alloy, J. Mater. Process. Technol. (2007) 644–647. https://doi.org/10.1016/j.jmatprotec.2006.08.010.
12. S.-H. Kim, B.-S. You, C. Dong Yim, Y.-M. Seo, Texture and microstructure changes in asymmetrically hot rolled AZ31 magnesium alloy sheets, Mater. Lett. 59 (2005) 3876–3880. https://doi.org/10.1016/j.matlet.2005.07.024.
13. B. Radhakrishnan, S.B. Gorti, G.M. Stoica, G. Muralidharan, A.D. Stoica, X.-L. Wang, E.D. Specht, E. Kenik, T. Muth, Mesoscale Modeling and Validation of Texture Evolution during Asymmetric Rolling and Static Recrystallization of Magnesium Alloy AZ31B, Metall. Mater. Trans. A 43 (2012) 1509–1516. https://doi.org/10.1007/s11661-011-0896-4.
14. W.J. Kim, J.B. Lee, W.Y. Kim, H.T. Jeong, H.G. Jeong, Microstructure and mechanical properties of Mg–Al–Zn alloy sheets severely deformed by asymmetrical rolling, Scr. Mater. 56 (2007) 309–312. https://doi.org/10.1016/j.scriptamat.2006.09.034.
15. E. Tolouie, R. Jamaati, Asymmetric cold rolling: A technique for achieving non-basal textures in AZ91 alloy, Mater. Lett. 249 (2019) 143–146. https://doi.org/10.1016/j.matlet.2019.04.087.
16. S.-B. Kang, B.-K. Min, H.-W. Kim, D.S. Wilkinson, J. Kang, Effect of asymmetric rolling on the texture and mechanical properties of AA6111-aluminum sheet, Metall. Mater. Trans. A 36 (2005) 3141–3149. https://doi.org/10.1007/s11661-005-0085-4.
17. N. El Mahallawy, A. Ahmed Diaa, M. Akdesir, H. Palkowski, Effect of Zn addition on the microstructure and mechanical properties of cast, rolled and extruded Mg–6Sn–xZn alloys, Mater. Sci. Eng. A 680 (2017) 47–53. https://doi.org/10.1016/j.msea.2016.10.075.
18. W. Cheng, Q. Tian, H. Yu, B.S. You, H. Wang, Optimum parameters and kinetic analysis for hot working of a homogenized Mg–8Sn–1Al–1Zn alloy, Mater. Des. 85 (2015) 762–770. https://doi.org/10.1016/j.matdes.2015.07.047.
19. Y.G. Ko, J. Suharto, J.S. Lee, B.H. Park, D.H. Shin, Effect of Roll Speed Ratio on Deformation Characteristics of IF Steel Subjected to Differential Speed Rolling, Met. Mater. Int. 19 (2013) 603–609. https://doi.org/10.1007/s12540-013-3033-7.
20. Y. Wang, J. Huang, Texture analysis in hexagonal materials, Mater. Chem. Phys. 81 (2003) 11–26. https://doi.org/10.1016/s0254-0584(03)00168-8.
21. R.K. Nadella, I. Samajdar, G. Gottstein, Static Recrystallisation and Textural Changes, Magnesium: Proceedings of the 6th International Conference Magnesium Alloys and Their Applications (2005) 1052–1057. https://doi.org/10.1002/3527603565.ch163.
22. J.F. Humphreys, Nucleation in Recrystallization, Mater. Sci. Forum. 467–470 (2004) 107–116. https://doi.org/10.4028/www.scientific.net/msf.467-470.107.
23. R.K. Sabat, N. Bibhanshu, G.S. Avadhani, S. Kumar, S. Kandalam, S. Suwas, Superplasticity in high temperature magnesium alloy WE43, Mater. Sci. Eng. A 687 (2017) 85–92. https://doi.org/10.1016/j.msea.2016.12.129.
24. A.N. Doğruoğlu, On constructing kinematically admissible velocity fields in cold sheet rolling, J. Mater. Process. Technol. 110 (2001) 287–299. https://doi.org/10.1016/s0924-0136(00)00897-9.
25. J. Sidor, A. Miroux, R. Petrov, L. Kestens, Microstructural and crystallographic aspects of conventional and asymmetric rolling processes, Acta Mater. 56 (2008) 2495–2507. https://doi.org/10.1016/j.actamat.2008.01.042.